Macrostructural changes in compacted earthen construction materials under loading

October 19, 2012

C.T.S. Beckett (corresponding author)
School of Civil and Resource Engineering,
University of Western Australia,
Crawley, WA 6009
christopher.beckett@uwa.edu.au

M.R. Hall
Nottingham Centre for Geomechanics,
Division of Materials, Mechanics and Structures,
Faculty of Engineering,
University of Nottingham,
University Park,
Nottingham, NG7 2RD, UK
matthew.hall@nottingham.ac.uk

C.E. Augarde
School of Engineering and Computing Sciences,
Durham University,
Durham, DH1 3LE, UK
charles.augarde@dur.ac.uk

Keywords: X-ray computed tomography, rammed earth, macrostructure, cracking

Abstract

There is increasing interest in the use of earthen materials for modern construction. The mechanical behaviour of these materials is strongly controlled by their internal macrostructures. Rammed earth (RE) is one example of these materials, created by *in situ* compaction of a wet soil mixture. Changes to the material structure occur on loading and during compaction; therefore, the nature of these changes needs to be understood if the effect on the material behaviour can be predicted. Here, the change in the macrostructure of RE on the application of compressive loading is investigated by using X-ray computed tomography and fractal analysis to monitor the changes in loaded RE specimens. The macrostructures of specimens comprising different layer thicknesses are also investigated in order to determine how layer thickness affects the compaction of the material. Results are used to recommend procedures for manufacturing specimens that are representative of the material found in full-scale RE structures.

1 Introduction

Rammed earth (RE) is the name given to an ancient building technique and an earthen construction material. Until recently, RE has been regarded as a material for which structural design was based on the experience of local craftsmen, much as masonry was regarded in the early 20^{th} century. However, the desire to use RE in new environments, encouraged by its inherent sustainability, low environmental impact and its ability to maintain comfortable living conditions, has prompted a new examination of the material as a compacted, highly unsaturated soil (Jaquin et al., 2009). In addition, the large number of heritage RE structures worldwide requiring conservation has prompted the search for better scientific understanding.

RE's behaviour is controlled by the internal structure of the material, namely the distribution of particles, pores and water and how these combine to form aggregates (Diamond, 1971; Collins and McGown, 1974; Tuller et al., 1999; Tarantino and De Col, 2008; Monroy et al., 2010; Zhang and Li, 2010; Beckett, 2011). Changes which occur to the internal structure therefore affect the behaviour of RE. Such changes can be due to cracking on the application of a load or due to the use of different compactive efforts in different regions of the material. It is therefore necessary to be able to predict how the material will change in order to know the subsequent effect on the material behaviour.

The process of cracking in rocks has been studied in some detail, however much less attention has been paid to sedimentary materials, for example RE (Dehandschutter et al., 2004, 2005). An understanding of the cracking process in soils has gained importance over recent years due to concerns associated with the burial of nuclear waste, for example, where heat-induced fracturing can lead to changes of permeability of the lining material and the escape of potentially-dangerous leachates (Gens et al., 2011). For dry soils, the application of a tensile or compressive load results in brittle failure through the formation, growth and joining of flaws within the soil structure (Atkinson, 1987). These flaws can either be the pores themselves or pre-existing cracks. Brittle failure of specimens at low water contents is well documented and is due to frictional failure and the breaking of liquid bridges at the interparticle contacts (Braunack et al., 1979; Rondeau et al., 2003; Dehandschutter et al., 2005; Baltodano-Goulding, 2010; Hoyos et al., 2010; Vallejo, 2010).

An RE layer is formed by compacting loose sandy-loam subsoil at its optimum water content (OWC) between formwork. However, due to friction with the sides of the formwork, the

compactive effort applied to material towards the top of the layer is greater than that towards the base (Morel et al., 2007). This can be mitigated slightly by the use of specially-shaped rammer heads (e.g. heart– or wedge-shaped), but a change in the compactive effort is still present, so that the material structure, and so its behaviour, varies throughout the layer thickness (Proctor, 1933; Betts and Miller, 1937). As these changes in behaviour can be detrimental to the structure (e.g. reduced strength or increased permeability), it is necessary to understand how compaction of different layer thicknesses affects the material structure so that appropriate thicknesses can be used.

Here, X-ray Computed Tomography (XRCT) is used to non-destructively investigate the change in the macrostructure of RE specimens on the application of a load. Specimens comprising different layer thicknesses are also examined in order to determine how layer thickness affects the compaction of the material.

2 X-ray computed tomography

Computerised tomography (CT) was developed in order to create 2-D or 3-D reconstructions of internal features of objects non-destructively (Roscoe, 1970; Wellington and Vinegar, 1987). XRCT is an improvement over CT which significantly increases the scanning resolution: current generation XRCT devices are able to achieve maximum resolutions of roughly 0.05 μm and resolutions of 10 μm for objects that are a few millimetres across (Rigby et al., 2011).

XRCT uses X-ray attenuation (the loss of energy as a ray passes through a material) to reconstruct images of the interior of an object (Keller, 1998). Radiographic projections (i.e. 2-D images acquired using X-rays) of the object are taken from many angles by rotating the object relative to a stationary X-ray source and detector. The X-ray attenuation is then calculated at specific points and the 2-D image or *slice* constructed. 3-D reconstruction of the object can be achieved by converting slice pixels into voxels and then "stacking" several slices on top of each other. The reader is referred to Kruth et al. (2011) for a detailed description of the XRCT process.

XRCT was first used with geotechnical materials to observe 2-D stress fields in sands (e.g. Roscoe (1970)). 3-D studies on strain localisation in sands have been conducted since the late 1980s, achieved using XRCT images and subsequent image analysis techniques (for example particle image velocimetry, as discussed in Beckett and Augarde (2011)) to track deformations

during loading (Colliat-Dangus et al., 1988; Van Geet et al., 2000; Desrues and Viggiani, 2004; Hall et al., 2010). XRCT has recently been used to characterise the hydration of clay pellets and powders (Van Geet et al., 2005; Gens et al., 2011).

Several imperfections which arise during XRCT scanning were identified by Van Geet et al. (2000):

- *Ring artifacts* are caused by inhomogeneities in the projector. They can be detected and accounted for by randomly moving the object relative to the detector.
- *Star artifacts* are caused by very dense inclusions within the object, radiating incident rays back out of the specimen. Star artifacts can be reduced by placing different filters in front of the projector, depending on the material causing the error.
- *Shadowing* occurs due to the absorbing of low-energy waves at the edges of objects. Again, the use of filters can prevent shadowing.

3 Fractal analysis

Fractal analysis can be used to describe the shapes and arrangements of irregular objects (Mandelbrot, 1967). As opposed to Euclidean geometry, where objects are classified as one, two or three dimensional, the dimensionality of an irregular line can take any value between one and two, with more irregular lines having larger *fractal dimensions*. As fractals quantify irregular structures, they are a suitable tool for quantifying the internal structure of RE and changes which occur to it. Fractals have been used to investigate several properties of geotechnical materials, for example in modelling particles and pore networks (Perfect et al., 1992; Lipiec et al., 1998; Perrier et al., 1999; Perrier and Bird, 2002; Atzeni et al., 2008), permeability (Thevanayagam and Nasarajah, 1998; Xu and Sun, 2002; Xu, 2004a; Cihan et al., 2009; Jobmann and Billaux, 2010) and retention curve properties (Bird et al., 1996; Gimnez et al., 1997; Kravchenko and Zhang, 1998; Huang et al., 2006; Russell, 2010). Fractals have also been used to describe soil cohesive properties (Bonala and Reddi, 1999) and unsaturated shear strength (Xu, 2004b).

The fractal dimension of a line can be found by dividing it into elements of length λ (known as the *dividing method*) and finding the number of such elements, $P(\lambda)$, that are required to cover the line. $P(\lambda)$ and λ are related by

$$P(\lambda) = k\lambda^{-D_f} \tag{1}$$

where k is a constant and D_f is the fractal dimension (Ersahin et al., 2006). D_f is found by plotting λ on the abscissa axis against $P(\lambda)$ on the ordinate axis using a logarithmic scale. The gradient of the resulting linear fit (necessary for the line to be considered fractal), m, is related to D_f via $D_f = -m$. The fractal dimension of a straight line or circular arc will always be 1 using this method (Vallejo, 1996).

The *box-counting method* overlays an object with parallel vertical and horizontal lines, separated by a distance λ (Hirata, 1989). Each "box" formed by the intersecting lines forms one element and $P(\lambda)$ is found by counting the number of boxes which contain part of the object, as shown in Figure 1. Successively fine grids are used to determine D_f from a plot of λ against $P(\lambda)$ as before. The accuracy of the estimate of D_f can be improved by choosing an appropriate range of values for λ and by using multiple grid locations, using the average of the number of boxes filled for each location to find D_f (Foroutan-pour et al., 1999). The *minimum cover* value for D_f is the fractal dimension calculated using the grid which requires the least number of elements to cover the object (Tolle et al., 2003). Therefore, if only one grid location is used, the average and minimum cover D_f values are the same. Like the dividing method, the fractal dimension for a straight line or circular arc found using the box-counting method will always be 1.

The fractal dimension gives a measure of the size and dispersivity of objects. However, D_f cannot indicate the amount of objects present in the pattern: therefore, an additional parameter is required to describe fractal patterns. The *lacunarity*, L, represents the interconnectivity (or heterogeneity or *gappiness*) of the pattern, and can be considered to be the $P(\lambda)$ intercept of the linear fit to the plot of λ against $P(\lambda)$. A larger value of L therefore indicates that there are more gaps between the objects so that a greater number of boxes is required to cover the pattern (Zeng et al., 1996). Both the lacunarity and the fractal dimension are therefore required to describe a fractal pattern (Pachepsky et al., 2000; Blair et al., 2007).

4 Experimental procedure

4.1 Soil mix selection and preparation

It is recommended that specimens be of the order of 1000 times larger than the desired resolution for XRCT scanning (Ketcham and Carlson, 2001). Specimens of 20 mm height and 15 mm diameter were selected in order to use a high scanning resolution (1 pixel to 11 μm) whilst being

large enough to be representative of material used in construction. Although a resolution of 11 μm is insufficient to investigate the smallest pores within the material (on the nanometre scale), it is suggestibly sufficient to determine structural changes due to crack formation. Therefore, that this study focuses on changes which occur to the material macrostructure (with pores identified necessarily belonging to the macropore class). As cracking in quasi-brittle materials, for example RE, is a macroscopic phenomenon, this resolution should be sufficient to determine the effects of loading and compaction on material macrostructure (Dehandschutter et al., 2005).

A soil mix comprising 70% sand and 30% silty-clay by mass was selected for testing. Although traditional RE soil mixes should contain a gravel fraction (Houben and Guillaud, 1996), the restriction on specimen size precludes the incorporation of large particles; the material investigated here can therefore be considered to be representative of the intra-aggregate (or "soil matrix") material, rather than the entire RE mix.

The mix was prepared by combining dry constituent materials in the appropriate proportions. Dried silty clay ("Birtley clay", LL 58.8%, PL 25.7%, PI 33.1%) was prepared by drying lumps of the material at 105°C for 48 hours (BS1377:1990), prior to being pulverised and passed through a 2.36 mm sieve. This sieve size was selected as particle aggregates were small enough to mix uniformly with the remaining mix fractions on the creation of the soil mix whilst producing a sufficient quantity of material at an acceptable rate. Dried sand was also sieved to pass 2.36 mm in order to remove gravel-sized particles (2–20 mm, BS1377:1990). The light Proctor test was used to determine the mix optimum water content (OWC); this was chosen as it is deemed representative of the compaction applied to full-scale RE structures (Beckett and Augarde, 2010). Material maximum bulk and dry densities and OWC are given in Table 1.

4.2 Specimen preparation and testing

Specimens were manufactured using the apparatus shown in Figure 2. The mould shown in Figure 2 is open at both ends to facilitate extraction; during manufacture, the mould was secured to a removable steel base plate (not shown in Figure 2). Twelve single– and three double-layer specimens were prepared for XRCT scanning. Consecutive testing on a single specimen, for example as performed by Hall et al. (2010) and Andò et al. (2012), was not possible due to limitations on scanner availability. This is acceptable as cracking within the material do not close on the removal of an applied load (Atkinson, 1987).

Wet material was prepared in a sealable polypropylene container in three layers of 2.5 kg,

wetted to OWC using distilled water. The container was treated with an anti-static cleaner prior to being filled with the dry soil mix to prevent dry clay particles from adhering to the container surfaces and sealed for 48 hours to allow the water to equilibrate. Single-layer specimens were manufactured using the single-layer press (Figure 2) and static compaction, with the amount of material required determined through the required density and known specimen volume. Double-layer specimens were manufactured by allocating half of the required material to each layer and compacting the first layer with the double-layer press and the second with the single-layer press.

Specimens were placed on wire racks to dry naturally to a constant mass at a temperature of 20°C ±2°C and a relative humidity of 40% ±5%. The porosities of the single– and double-layer specimens were 0.290 (standard deviation of 0.006) and 0.263 (standard deviation of 0.001) respectively, determined from the specimen mass, dry density and volume on reaching a constant water content. Two single-layer and two double-layer specimens (numbers 2s, 10s, 13d and 15d, where "s" and "d" denote single– and double-layer specimens respectively) were selected for XRCT testing as they had the most similar dry masses and so, assumedly, similar material structures. The remaining specimens were used to determine the unconfined compressive strength (UCS) of the material by being crushed between low-friction plattens at a set displacement rate of 0.5 mm/min. The average specimen compressive failure load was 287.4 N ±4.2 %, corresponding to an average UCS of 1.63 MPa, calculated as the applied load over the specimen cross-sectional area. Correction factors for the compressive strength based on the specimen aspect ratio have been suggested by a number of authors (e.g. Krefeld (1938) and Heathcote and Jankulovski (1992)), however it is suggested in Morel et al. (2007) that they are not suitable for use with earthen materials; UCSs have therefore been left unmodified.

Formwork used in RE construction is usually limited to 1.5 m high, in order to facilitate its movement around the site (King, 1996). If it is assumed that the wet density RE is roughly 2.1 Mg/m^3 (following results from Beckett and Augarde (2011)) and a layer, once compacted, is roughly 100 mm deep, then it can be shown that the bottommost layer is subjected to a load of roughly 29 kN/m^2 due to the material self weight, or roughly 2% of the average UCS reported above. As this is very small, it can be assumed that no significant cracking occurs due to material self weight. Therefore, the macrostructures of small specimens, as opposed to samples taken from a larger wall, should be adequate to determine changes which occur to the macrostructure of material present in full-scale RE walls on loading. Loads corresponding to

85% and 25% of the average failure load were then applied to specimens 2s and 10s respectively; these values were selected to provide a sufficient difference between their loaded macrostructures whilst enabling specimens to be safely transported. Specimens 13d and 15d were not loaded. A summary of these specimen preparation stages is given in Table 2

5 Results and discussion

5.1 Image processing

XRCT images were obtained using a Phoenix Nanotom 180NF XRCT system (GE Sensing and Inspection Technologies, GmbH, Wunsdorf, Germany) at a resolution of 1 pixel = 11 μm. Each set of projection images was reconstructed using the back projection algorithm in the "datos|x rec" software. "ImageJ v.1.43u" software (Rasband, 2002) was then used to process the XRCT images.

Examples of the 3-D detected pore networks, determined using the IsoData thresholding values given in Table 2 and produced using the AvizoFire software (Visual Sciences Group, Burlington, USA), are shown in Figures 3 and 4, which give an impression as to the highly complex nature of the macropore spaces within these specimens. Due to this complexity, 2-D image slices, rather than 3-D interpolations, are used here to determine changes that occur to the macrostructure on loading, using the procedures discussed above. An example of such a slice is shown in Figure 5(a), along with the specimen axes as defined by the XRCT scanning software, as well as the image prior to and post-processing using ImageJ; pores are shown as black pixels in the processed images, whilst solid material is shown as white. Example outlines of particles seen in Figure 5(b) are shown in Figure 5(c) for reference. Slices in the XY plane are used as this is the plane perpendicular to compaction, and it is expected that macrostructural changes will occur with depth, but not in the radial direction. The image processing procedure is given in Figure 6.

Images are divided into pore spaces and solid material using a threshold intensity value; the lower the value, the lower the pixel intensity (i.e. the darker the shade) that corresponds to pores. In order to prevent shadowing, the upper and lower 100 images, corresponding to the upper and lower 1.1 mm, were removed from the image sequence. The removal of these images also reduces the chance of any damaged material, likely to be found at the ends of the specimen, from influencing the analysis. Failure to remove these images results in a lower thresholding

value being selected, so that fewer pores are identified. Roughly 1600 images in the XY plane were therefore subsequently available for analysis per specimen, at 11 μm intervals. An area of 938 $\times$ 856 pixels was cropped from the centre of XY-orientated images to avoid shadowing at the specimen edges and to provide a constant cross sectional area for the analysis. Due to the large number of images, only one in every ten images (i.e. one image every 110 μm) was processed.

For thresholding, original image brightness values were modified whereby the lowest intensity present in the image was set to zero and the highest to 255 (the minimum and maximum possible intensity values respectively), in order to ensure the greatest contrast between pixels. A "median" filter was then applied in order to reduce the noise in the image by removing outlying intensity regions. This method replaces a pixel's intensity with the median intensity of a region of a given size centred on that pixel (a region of a 2 pixel radius was used in this case). The brightness values were then corrected again, using the process described above, to account for the filtering process. The ImageJ "IsoData" thresholding algorithm was applied to the modified images to determine a suitable thresholding value.

The IsoData process divides the image into pores and solids using an initial threshold value. The average intensities of those pixels whose intensities are above and below that value are then calculated and the average of those is used as a second threshold value. The process is repeated until the calculated threshold is larger than the average intensity for the entire image (Ridler and Calvard, 1978). Double-layer specimens, although their layers were scanned separately, were analysed as one image sequence in order to directly compare one layer to another. Final IsoData threshold values are given in Table 2, with the same thresholding value being applied to every image in the image sequence. Values differ between specimens due to the manual brightness correction procedure and subtle differences in their structure (e.g. particle mineralogy) which influence that correction.

5.2 Effect of loading on material macrostructure

Results found for specimens 2s and 10s were used to determine the effect of loading on material macrostructure. Preliminary testing indicated that the use of five grid positions with a minimum box size of 1 pixel gave the most repeatable results for macrostructure fractal properties using the minimum cover box counting method. The Pore Area Fraction (PAF, calculated by dividing the detected pore area by the total image area), fractal dimension, D_f, and lacunarity, L, calculated

for each specimen using the processed images, for a range of tested image thresholding values, are shown in Figures 7 to 9 respectively. Depths have been calculated assuming a 110 μm separation between images and have been corrected to account for the 1.1 mm of material removed from the top and bottom of the image sequence. To prevent the loss of loose particles from the base of the specimens and to ensure a good seating within the scanner, specimens were placed in the scanner with the topmost compacted surface (which is the smoothest) facing *downwards*. Therefore, a depth of 0 in Figures 7 to 9 corresponds to the *base* of the specimen. A minimum pore size of 3×3 pixels (i.e. $\geq 1089 \mu m^2$) was used to calculate the PAF in order to prevent anomalous features (for example small pits on particle surfaces or random image noise) from influencing the results, however a minimum box size of 1 pixel was used to determine D_f and L (i.e. features $\geq 121 \mu m^2$ are included in the fractal analysis).

Figures 7 and 8 show a good level of continuity between consecutive values of PAF and D_f found using IsoData thresholding intensity, suggesting that a resolution of 11 μm is suitable for investigating the macrostructures of these materials. These figures also show a sudden increase in PAF and D_f, for both specimens, at depths near 0 and 20 mm. However, Figures 10(a) and (b), taken at depths of 16500 μm and 17379 μm respectively for specimen 2s (i.e. corresponding to regions just below and at the tip of these sudden increases), show very little apparent difference between their macrostructures. These sudden increases are therefore suggested to be indicative of shadowing, whereby slightly darker image at the specimen edges give unrealistically large detected pore areas as compared to images taken from the bulk of the specimen. Ignoring these shadowed regions, the maximum measured PAFs detected for specimens 2s and 10s at the IsoData threshold value are roughly 0.16 and 0.14 respectively, which are significantly smaller than their average bulk porosities of 0.29. This is again indicative of how XRCT can only be used to gain information about the material macrostructure using this resolution.

IsoData values shown in Figure 7 clearly indicate that PAF, and so by extension macrostructural density and material strength (Hall and Djerbib, 2004), increases with increasing depth (i.e. towards the top of the specimen). A slight reduction in D_f and an increase in L is also seen in Figures 8 and 9 with increasing depth, suggesting that detected macropores become elongated and more isolated, supporting the observation that the material is more heavily compacted towards the top of the specimen. This is unexpected, as the small depth of the layer would suggestibly be sufficient to ensure uniform compaction throughout the material. Instead, results suggest that friction with the sides of the mould results in this decreasing density to-

wards the specimen base (Morel et al., 2007). Whether such a result would occur in full-scale RE formwork (of the order of 300 mm wide) is unclear, due to the different friction conditions and significantly larger volumes involved, however it is clear that care should be taken to ensure that specimen compaction results in a similar material to that found on-site.

The nature of the macrostructures of specimens 2s and 10s can be investigated in more detail by varying the threshold values (low thresholding values detect the darkest pixels and so the centres of the largest pores, whilst smaller pores are detected as the value is increased), as the arrangement of large and small detected macropores can be determined (Taud et al., 2005). An example of the use of different threshold intensities to investigate an image slice is shown in Figure 11. Detected PAF, D_f and L values using different threshold intensities are also shown in Figures 7 to 9 (selected intensities are shown in parentheses in the figure legends). Threshold values below 50 were not examined as no pores could be detected in some images. Similarly, values larger than the IsoData threshold values (Table **??**) were not investigated as some images became completely populated by pores.

Figure 7 shows that higher values of PAF and D_f, and lower values of L, are largely observed for specimen 2s than for specimen 10s at all investigated threshold intensity values and sample depths. An increasing D_f and reducing L with increasing threshold value is indicative of smaller pores residing between, and not in isolation of, larger pores, so that smaller features (macropores and cracks) propagate from larger features. The similar trends for PAF, D_f and L for both specimens suggest that their initial macrostructures were similar, so that the differences between them are due to the application of differing loads only. Therefore, results shown in Figures 7 to 9 for different threshold values suggest that the application of a load to the initial macrostructure affects the entire pore size range investigated, and that it results in the formation and propagation of cracks from the larger to the smaller pores. This has important consequences for considerations of hydraulic conductivity, for example, as increasing pore interconnectivity will result in increased conductivity.

As results discussed above suggest that the initial macrostructures of specimens 2s and 10s were indeed similar, the extent by which pores of different sizes are affected by loading can be determined by examining the relative changes in PAF, D_f and L between specimens at given depths. Figures 12 to 14 show the percentage differences between PAF, D_f and L for the two

specimens respectively, calculated using

$$\frac{\text{value 2s} \; - \; \text{value 10s}}{\text{value 2s}} \; \times \; 100. \tag{2}$$

Note that Eqn **??** removes the effect of shadowing. Although PAF reduces with increasing sample depth (Figure 7), Figure 12 shows that, with some oscillations (which are discussed below), the relative change in PAF between the two samples is relatively constant for a given depth at around +30% for all threshold intensities, suggesting that pores of all sizes were equally affected by the application of a load. By extension, this suggests that material compacted to a lower density will experience greater cracking than the same material compacted to a higher density, due to the greater number of pre-existing flaws. This is consistent with the theory of cracking of quasi-brittle materials, as it is expected that a greater number of cracks can propagate from larger initial flaws (Atkinson, 1987). Figures 13 and 14 show that IsoData values of D_f and L remained relatively constant at +5% and −50% respectively, again indicating that flaws (macropores and cracks) become larger and more interconnected on the application of a load and again consistent with the above theory. A greater variation in relative PAF, D_f and L values is seen for lower threshold values; this is due to the more isolated arrangements of the identified features at these intensity values, again as shown in Figure 11.

Figures 12 and 13 show several oscillations in obtained results between depths of 0 and roughly 12 mm, due to similar oscillations seen in Figures 7 and 8. As the oscillations for each specimen are not in phase with each other with depth, which would suggest a material property, this instead suggests that errors were encountered whilst moving the specimen relative to the X-Ray source and receptor, perhaps due to an incomplete isolation of the specimen from external light. However, it is assumed here that these errors do not detract from the usefulness of the data to determine structural changes on the application of a load.

Figures 12 and 13 show a large shift to negative relative PAF and D_f values between the depths of 12 and 17 mm, due to an increase in PAF and D_f of specimen 10s between these depths, apparently contradicting results discussed above. An image slice taken from this region of sample 10s (at a depth of 13090 μm) is shown in Figure 11, showing that a large particle (roughly 10 mm) is present at this depth which was not removed during sieving. The effect of this particle is to reduce the compactivity of that material adjacent to it, as shown in Figures 7 and 8 through the increase in PAF and D_f in this region. A considerable increase in L is

also seen in this depth range, due to the large 'gap' which the particle represents. It should be noted, however, that although the relative differences between specimens 2s and 10s in this region are large, the absolute differences, as shown in Figures 12 to 14, are quite small as compared to the largest values determined (for example, the highest PAF found for specimen 10s, excluding shadowed areas, is roughly 15%, whereas PAF in the region containing the large ranges between only 5 and 10%). Results found for specimen 10s are therefore suggestibly still valid for determining the effects of loading on material macrostructure, although relative values are misrepresentative of these effects in the region of the large particle.

5.3 Effect of compaction on the material macrostructure

Specimens 13d and 15d were used to investigate changes which occur to material macrostructure on the compaction of additional layers. Values of PAF, D_f and L determined for each specimen using different threshold values are shown in Figures 15 to 17 respectively. Again, a depth of 20 mm corresponds to the *top* of the specimen due to its orientation in the XRCT scanner.

Opposite to Figures 7 and 8, Figures 15 and 16 show reduced PAF and D_f values at the ends and in the centres of the specimens, whilst Figure 17 shows higher L values at the specimen ends, suggesting that images taken from these regions were in fact darker than those taken from the bulk of the material (i.e. a *reversed* shadowing effect, as a darker image returns a greater number of detected pores). PAF and D_f values in Figures 15 and 16 are also significantly higher than those shown in Figures 7 and 8, suggesting that the majority of the space in the image slices has been incorrectly classified as pore space (as a PAF value of 1, or D_f value of 2, represents a rectangular area entirely comprising pore space). These results suggest that the IsoData thresholding method is inappropriate for analysing these specimens. Examples of the use of different thresholding values on detected pore area are shown in Figure 18; although The IsoData threshold value results in a realistic approximation to the pore network shown in Figure 18(a) (taken from the top of the specimen, depth 1100 μm) in Figure 18(c), it severely overestimates the pore area of Figure 18(d) (taken from the bulk material, depth 17600 μm) in Figure 18(f), and hence produces the drops in PAF and D_f values seen at the specimen ends and centre in Figures 15 and 16.

Due to the unrealistic PAF and D_f and L values obtained using the IsoData threshold value, images were re-analysed using a lower threshold value of 60 (chosen following preliminary work). These results are also shown in Figures 15 to 17. Figure 18 shows that the use of

the lower threshold intensity of 60 produces a far better approximation to the pore network in Figure 18(b), but fails to capture most of the pores in Figure 18(e). Given that results discussed in the previous section show that results for the uppermost and lowermost material should be discounted due to shadowing (or the apparent 'reversed shadowing' in this case), the use of a threshold value of 60 appears to be the more appropriate for investigating changes to the macrostructure on layer compaction.

Figures 15 to 17 show relatively good agreement between PAF, D_f and L values determined using the threshold value of 60 for both specimens, suggesting that their macrostructures are quite similar and so that results for both can be used to investigate the effects of layer compaction on material macrostructure. The effect of shadowing detected at this threshold value is also consistent with that found in Figures 7 to 9 (i.e. an increase in the number of detected pores at the edges), suggesting that the 'reversed' shadowing in Figures **??** to **??** was indeed due to the use of too high a threshold value. As in Figures 12 and 13, oscillations are also seen in Figures 15 and 16 for changing PAF and D_f with depth respectively. However, these oscillations are in phase with each other for specimens 13d and 15d, again suggesting that they are due to an error encountered whilst moving specimens within the scanner during the analysis and not due to a change in the macrostructure. This further suggests that the change in the phase of these oscillations between results for specimens 2s and 10s in Figures 15 and 16 is the result of a change in the macrostructures of those specimens due to loading.

A considerable change in seen in the values found for PAF, D_f and L for both specimens at a depth of roughly 9 mm in Figures 15 to 17, whereby material in the upper layer has considerably higher PAF and D_f values and lower L values than that in the bottom layer, so that the material in the upper layer is characterised by larger macropores with a higher degree of interconnectivity. This is supported by Figure 19, which shows a central section, in the XZ plane, through sample 13d and which clearly shows that the upper compacted layer has a significantly higher porosity than the lower layer (layers are indicated by boxes in Figure 19). Of interest, however, is the placement of the layer interface at a depth of 9 mm from the uppermost surface, as opposed to the intended 10 mm. If this were due to the additional compaction of the underlying layer, then it would be expected, following results seen in Figure 7, that a density gradient would be observed throughout the layer, with density reducing with increasing layer depth. The identical depths of the layer interfaces in both specimens would also not be expected if the change in material structure were due to the additional compaction of the underlying layer.

These observations therefore suggest that the significant difference in the macrostructures of the two layers is due to an error in the length of the double-layer press, in that it was infact 11 mm, as opposed to the intended 10 mm, which resulted in an over-compaction of the specimen material in the bottom layer, due to the use of a set mass of material, and a subsequent under compaction of the material in the upper layer. This therefore suggests that the macrostructure of the material in the underlying layer was not, in fact, affected by the compaction of the material above it, supporting results presented in (Beckett and Augarde, 2011), although further testing is required to confirm this due to the under-compacted nature of the upper layer. Therefore, the result found in the previous section that macrostructural density reduces, with an associated increase in macropore size and interconnectivity, towards the base of a compacted layer can be applied to every layer within an RE structure.

Morel et al. (2007) observed that compressive strength correction factors for different aspect ratios determined for masonry materials are not suitable for soils, as the material is not homogeneous throughout the layer. However, they assumed that the material comprising specimens with aspect ratios below 1.5 can be considered homogeneous, so that existing correlation factors might be acceptable. Furthermore, the specification of an aspect ratio does not place limitations on any one dimension of a specimen, depending on the values of the other dimensions. Results presented here show that the material comprising the tested single-layer samples (aspect ratio $\frac{4}{3}$) is highly heterogeneous, with largely homogeneous material only observed in the even shallower double-layer specimen layers (aspect ratio $\frac{2}{3}$, although the compaction applied to these layers is suspect). Therefore, it is suggested that layer thickness, and by extension the relation between that and maximum particle size, be considered when determining the degree of homogeneity of RE materials as opposed to specimen aspect ratio.

6 Conclusion and recommendations

The aims of this investigation were to use XRCT scanning to observe the changes that occurred to the macrostructure of RE on loading and to determine how the the macrostructure changed throughout a layer as a result of compaction.

Results presented for all specimens suggest that an XRCT scanning resolution of 11 μm is sufficient to investigate macrostructural properties of RE materials. Results for single-layer specimens have shown that the application of a load to an RE material results in a significant

increase in the size and interconnectivity of macropores due to cracking, with the degree of cracking increasing for larger loads. It was also shown that the effect of cracking was greater for larger macropores than for smaller, due to the greater number of cracks that can propagate from the larger. Therefore, poorly-compacted material will suffer more cracking than well-compacted material for the same applied load, indicating the need for proper compaction during construction.

Results for single-layer specimens show that macrostructural density continuously reduces towards the base of a compacted layer. It is therefore likely that material found at the bottom of a compacted layer is weaker than that at the top, with a higher hydraulic conductivity due to increased pore size and interconnectivity.

Results found for double-layer specimens have shown that the macrostructure of a compacted layer is not affected by the compaction of additional material above it. Therefore, properties of RE specimens comprising few compacted layers can be considered to be representative of material contained within full-scale RE structures, although layer thickness should be similar to that found in the full-scale structure due to the variations in material density with layer depth identified above.

Results for single-layer specimens show that the macrostructure of material comprising a compacted layer is highly heterogeneous, with largely homogeneous material only found in the layers of double-layer specimens. Care should therefore be taken when specifying minimum specimen aspect ratios to achieve material homogeneity. Instead, limitations should be placed on specimen layer thickness and maximum particle size.

7 Acknowledgements

The first author is supported by a studentship awarded by the School of Engineering and Computing Sciences, Durham University.

References

Andò, E., Hall, S., Viggiani, G., Desrues, J., Bésuelle, P., 2012. Grain-scale experimental investigation of localised deformation in sand: a discrete particle tracking approach. Acta Geotechnica 7 (1), 1–13.

Atkinson, B. K. (Ed.), 1987. Fracture mechanics of rock. Academic Press Inc., London (UK).

Atzeni, C., Pia, G., Sanna, U., Spanu, N., 2008. A fractal model of the porous microstructure of earth-based materials. Construction and Building Materials 22 (8), 1607–1613.

Baltodano-Goulding, R., September 2010. Deformation behavior in unsaturated soils. In: Alonso, E., Gens, A. (Eds.), Unsaturated Soils. Fifth International Conference on Unsaturated Soils, CRC Press, pp. 181–185.

Beckett, C. T. S., 2011. The role of material structure in compacted earthen building materials: Implications for design and construction. PhD Thesis, Durham University.

Beckett, C. T. S., Augarde, C. E., September 2010. Development of microstructure in compacted earthen building materials. In: Alonso, E., Gens, A. (Eds.), Unsaturated Soils. Fifth International Conference on Unsaturated Soils, CRC Press, pp. 139–144.

Beckett, C. T. S., Augarde, C. E., 2011. A novel image-capturing technique for the experimental study of soil deformations under compaction. Geotechnical Testing Journal 34 (6), 571–578.

Betts, M. C., Miller, T. A. H., 1937. Rammed earth walls for buildings. Farmers Bulletin No. 1500. U.S. Department of Agriculture, Washington D.C. (U.S. Govt. Printing Office).

Bird, N., Bartoli, F., Dexter, A., 1996. Water retention models for fractal soil structures. European Journal of Soil Science 47, 1–6.

Blair, J. M., Falconer, R. E., Milne, A. C., Young, I. M., Crawford, J. W., 2007. Modeling three-dimensional microstructure in heterogeneous media. Soil Science Society of America Journal 71 (6), 1807–1812.

Bonala, M. V. S., Reddi, L. N., 1999. Fractal representation of soil cohesion. Journal of Geotechnical and Geoenvironmental Engineering 125 (10), 901–904.

Braunack, M. V., Hewitt, J. S., Dexter, A. R., 1979. Brittle fracture of soil aggregates and compaction of aggregate beds. Journal of Soil Science 30, 653–667.

519 BSI, 1990. BS 1377:1990. Methods of test for soils for civil engineering purposes.

520 Cihan, A., Tyner, J. S., Perfect, E., 2009. Predicting relative permeability from water retention:
521 A direct approach based on fractal geometry. Water Resources Research 45, 8.

522 Colliat-Dangus, J. L., Desrues, J., Foray, P., 1988. Triaxial testing of granular soil under elevated
523 cell pressure. In: Donaghe, R. T., Chaney, R. C., Silver, M. L. (Eds.), Proceedings of a
524 conference on advanced triaxial testing for soil and rocks. American Society for Testing and
525 Materials, Philadelphia (USA), pp. 290–310.

526 Collins, K., McGown, A., 1974. Form and function of microfabric features in a variety of natural
527 soils. Géotechnique 24 (2), 223–254.

528 Dehandschutter, B., Vandycke, S., Sintubin, M., Vandenberghe, N., Gaviglio, P., Sizun, J. P.,
529 Wouters, L., 2004. Microfabric of fractured boom clay at depth: a case study of brittle-ductile
530 transitional clay behaviour. Applied Clay Science 26 (1-4), 389–401.

531 Dehandschutter, B., Vandycke, S., Sintubin, M., Vandenberghe, N., Wouters, L., 2005. Brittle
532 fractures and ductile shear bands in argillaceous sediments: inferences from oligocene boom
533 clay (belgium). Journal of Structural Geology 27 (6), 1095–1112.

534 Desrues, J., Viggiani, G., 2004. Strain localization in sand: an overview of the experimental
535 results obtained in grenoble using stereophotogrammetry. International Journal for Numerical
536 and Analytical Methods in Geomechanics 28, 279–321.

537 Diamond, S., 1971. Microstructure and pore structure of impact-compacted clays. Clays and
538 Clay Minerals 19, 239–249.

539 Ersahin, S., Gunal, H., Kutlu, T., Yetgin, B., Coban, S., 2006. Estimating specific surface area
540 and cation exchange capacity in soils using fractal dimension of particle-size distribution.
541 Geoderma 136 (3-4), 588–597.

542 Foroutan-pour, K., Dutilleul, P., Smith, D. L., 1999. Advances in the implementation of the
543 box-counting method of fractal dimension estimation. Applied Mathematics and Computation
544 105 (2–3), 195–210.

545 Gens, A., Valleján, B., Sánchez, M., Imbert, C., Villar, M. V., Van Geet, M., 2011. Hydrome-
546 chanical behaviour of a heterogeneous compacted soil: experimental observations and mod-
547 elling. Géotechnique 61 (5), 367–386.

548 Gimnez, D., Perfect, E., Rawls, W. J., Pachepsky, Y., 1997. Fractal models for predicting soil
549 hydraulic properties: a review. Engineering Geology 48 (3-4), 161–183.

550 Hall, M., Djerbib, Y., 2004. Rammed earth sample production: context, recommendations and
551 consistency. Construction and Building Materials 18 (4), 281–286.

552 Hall, S. A., Bornert, M., Desrues, J., Pannier, Y., Lenoir, N., Viggiani, G., Bésuelle, P., 2010.
553 Discrete and continuum analysis of localised deformation in sand using x-ray μct and volu-
554 metric digital image correlation. Géotechnique 60 (5), 315–322.

555 Heathcote, K., Jankulovski, E., 1992. Aspect ratio correction factors for soilcrete blocks. Aus-
556 tralian civil engineering transactions CE34 (4: Australia: Institution of Engineers), 309–312.

557 Hirata, T., 1989. Fractal dimension of fault systems in Japan: Fractal structure in rock fracture
558 geometry at various scales. Pure and Applied Geophysics 131, 157–170.

559 Houben, H., Guillaud, H., 1996. Earth construction - a comprehensive guide., Second Edition.
560 Intermediate Technology Publications, London (UK).

561 Hoyos, L. R., Pérez-Ruiz, D., Puppala, A. J., 2010. Constitutive modeling of unsaturated soil
562 behavior using a refined suction-controlled true triaxial cell: Preliminary observations. In:
563 Alonso, E., Gens, A. (Eds.), Unsaturated Soils. Fifth International Conference on Unsaturated
564 Soils, CRC Press.

565 Huang, G.-H., Zhang, R.-D., Huang, Q.-Z., 2006. Modeling soil water retention curve with a
566 fractal method. Pedosphere 16, 137–146.

567 Jaquin, P. A., Augarde, C. E., Gallipoli, D., Toll, D. G., 2009. The strength of unstabilised
568 rammed earth materials. Géotechnique 59 (5), 487–490.

569 Jobmann, M., Billaux, D., 2010. Fractal model for permeability calculation from porosity and
570 pore radius information and application to excavation damaged zones surrounding waste
571 emplacement boreholes in opalinus clay. International Journal of Rock Mechanics and Mining
572 Sciences 47 (4), 583–589.

573 Keller, A., 1998. High resolution, non-destructive measurement and characterization of fracture
574 apertures. International Journal of Rock Mechanics and Mining Sciences 35 (8), 1037–1050.

575 Ketcham, R. A., Carlson, W. D., 2001. Acquisition, optimization and interpretation of x-ray
576 computed tomographic imagery: Applications to the geosciences. Computers and Geosciences
577 27, 381–400.

578 King, B., 1996. Buildings of Earth and Straw: Structural Design for Rammed Earth and Straw-
579 Bale Architecture. Ecological Design Press, Sausalito, California (USA).

580 Kravchenko, A., Zhang, R., 1998. Estimating the soil water retention from particle-size distri-
581 butions: a fractal approach. Soil Science 163 (3), 171–179.

582 Krefeld, 1938. Effect of shape of specimen on the apparent compressive strength of brick ma-
583 sonry. In: Proceedings of the American Society of Materials, Philadelphia, USA. pp. 363–369.

584 Kruth, J., Bartscher, M., Carmignato, S., Schmitt, R., Chiffre, L. D., Weckenmann, A., 2011.
585 Computed tomography for dimensional metrology. CIRP Annals - Manufacturing Technology
586 60 (2), 821 – 842.

587 Lipiec, J., Hatano, R., Slowinska-Jurkiewicz, A., 1998. The fractal dimension of pore distribution
588 patterns in variously-compacted soil. Soil and Tillage Research 47 (1-2), 61–66.

589 Mandelbrot, B. B., 1967. How long is the coast of Great Britain? Statistical self-similarity and
590 the fractional dimension. Science 156, 636–638.

591 Monroy, R., Zdravkovic, L., Ridley, A., 2010. Evolution of microstructure in compacted London
592 clay during wetting and loading. Géotechnique 60, 105–199.

593 Morel, J.-C., Pkla, A., Walker, P., 2007. Compressive strength testing of compressed earth
594 blocks. Construction and Building Materials 21 (2), 303–309.

595 Pachepsky, Y. A., Gimnez, D., Crawford, J. W., Rawls, W. J., 2000. Conventional and fractal
596 geometry in soil science. In: Y. Pachepsky, J. C., Rawls, W. (Eds.), Fractals in Soil Science.
597 Vol. Volume 27. Elsevier, pp. 7–18.

598 Perfect, E., Rasiah, V., Kay, B. D., 1992. Fractal dimensions of soil aggregate-size distributions
599 calculated by number and mass. Journal of the Soil Science Society of America 56, 1407–1409.

600 Perrier, E. M. A., Bird, N. R. A., 2002. Modelling soil fragmentation: the pore solid fractal
601 approach. Soil & Tillage Research 64, 91–99.

Perrier, E. M. A., Bird, N. R. A., Rieu, M., 1999. Generalizing the fractal model of soil structure: the poresolid fractal approach. Geoderma 88, 137–164.

Proctor, R. R., 1933. Fundamental principles of soil compaction. Engineering News Record 111 (9), 245–248.

Rasband, W., 2002. NIH Image J.
URL `http://rsbweb.nih.gov/ij/index.html (verified 02.08.2011)`

Ridler, T. W., Calvard, S., 1978. Picture thresholding using an iterative selection method. Systems, Man and Cybernetics, IEEE Transactions on 8 (8), 630 –632.

Rigby, S. P., Chigada, P. I., Wang, J., Wilkinson, S. K., Bateman, H., Al-Duri, B., Wood, J., Bakalis, S., Miri, T., 2011. Improving the interpretation of mercury porosimetry data using computerised x-ray tomography and mean-field dft. Chemical Engineering Science 66 (11), 2328 – 2339.

Rondeau, X., Affolter, C., Komunjer, L., Clausse, D., Guigon, P., 2003. Experimental determination of capillary forces by crushing strength measurements. Powder Technology 130 (1-3), 124–131.

Roscoe, K. H., 1970. The influence of strains in soil mechanics. Géotechnique 20 (2), 129–170.

Russell, A. R., 2010. Water retention characteristics of soils with double porosity. European Journal of Soil Science 61 (3), 412–424.

Tarantino, A., De Col, E., 2008. Compaction behaviour of clay. Géotechnique 58 (3), 199–213.

Taud, H., Martinez-Angeles, R., Parrot, J., Hernandez-Escobedo, L., 2005. Porosity estimation method by x-ray computed tomography. Journal of Petroleum Science and Engineering 47 (3–4), 209–217.

Thevanayagam, S., Nasarajah, S., 1998. Fractal model for flow through saturated soils. Journal of Geotechnical and Geoenvironmental Engineering 124 (1), 53–66.

Tolle, C. R., Mcjunkin, T. R., J., G. D., 2003. Suboptimal minimum cluster volume cover-based method for measuring fractal dimension. In: IEEE Transaction on Pattern Analysis and Machine Intelligence. pp. 32–41.

629 Tuller, M., Or, D., Dudley, L. M., 1999. Adsorption and capillary condensation in porous media:
630 Liquid retention and interfacial configurations in angular pores. Water Resour. Res. 35 (7),
631 1949–1964.

632 Vallejo, L. E., 1996. Fractal analysis of the fabric changes in a consolidating clay. Engineering
633 Geology 43 (4), 281–290.

634 Vallejo, L. E., 2010. Compressive strength of unsaturtated fissured clays. In: Alonso, E., Gens,
635 A. (Eds.), Unsaturated soils. Fifth International Conference on Unsaturated Soils, CRC Press,
636 pp. 387–390.

637 Van Geet, M., Swennen, R., Wevers, M., 2000. Quantitative analysis of reservoir rocks by
638 microfocus x-ray computerised tomography. Sedimentary Geology 132 (1-2), 25–36.

639 Van Geet, M., Volckaert, G., Roels, S., 2005. The use of microfocus x-ray computed tomography
640 in characterising the hydration of a clay pellet/powder mixture. Applied Clay Science 29 (2),
641 73–87.

642 Wellington, S. L., Vinegar, H. J., 1987. X-ray computerized tomography. Journal of Petroleum
643 Technology, 885–898.

644 Xu, Y. F., 2004a. Calculation of unsaturated hydraulic conductivity using a fractal model for
645 the pore-size distribution. Computers and Geotechnics 31 (7), 549–557.

646 Xu, Y. F., 2004b. Fractal approach to unsaturated shear strength. Journal of Geotechnical and
647 Geoenvironmental Engineering 130 (3), 264–273.

648 Xu, Y. F., Sun, D. A., 2002. A fractal model for soil pores and its application to determination
649 of water permeability. Physica a-Statistical Mechanics and Its Applications 316 (1-4), 56–64.

650 Zeng, Y., Gantzer, C. J., Payton, R. L., Anderson, S. H., 1996. Fractal dimension and lacunarity
651 of bulk density determined with X-ray computed tomography. Soil Science Society of America
652 Journal 60 (6), 1718–1724.

653 Zhang, L. M., Li, X., 2010. Microporosity structure of coarse granular soils. J. Geotech. and
654 Geoenvir. Engrg. 136 (10), 1425–1436.

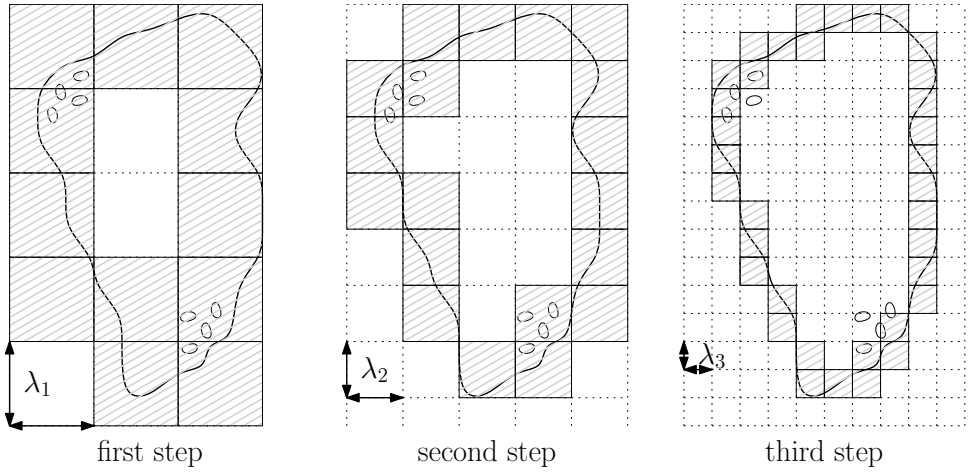

Figure 1: Box-counting method for determining particle profile fractal dimension. Hatching indicates those boxes that contain segments of the particle profile.

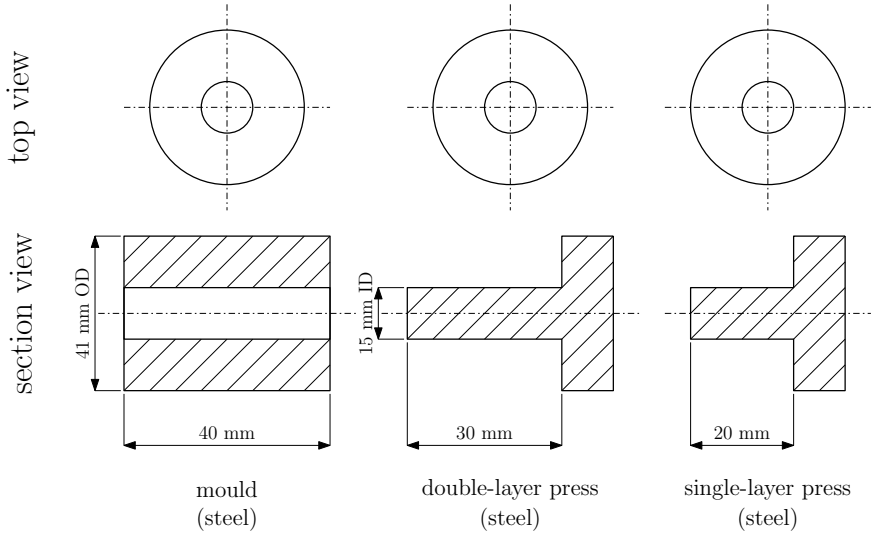

Figure 2: Sketch of the mould (left) and presses (middle and right) used for specimen preparation

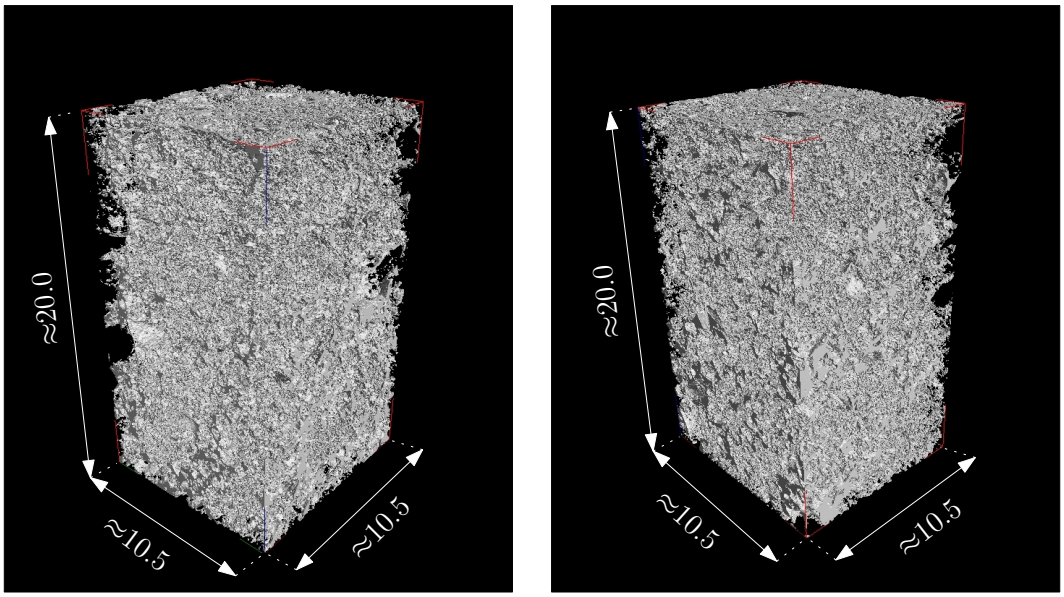

(a) (b)

Figure 3: Reconstructed 3-D pore network for single-layer specimens as detected using XRCT IsoData thresholding: a) specimen 2s; b) specimen 10s

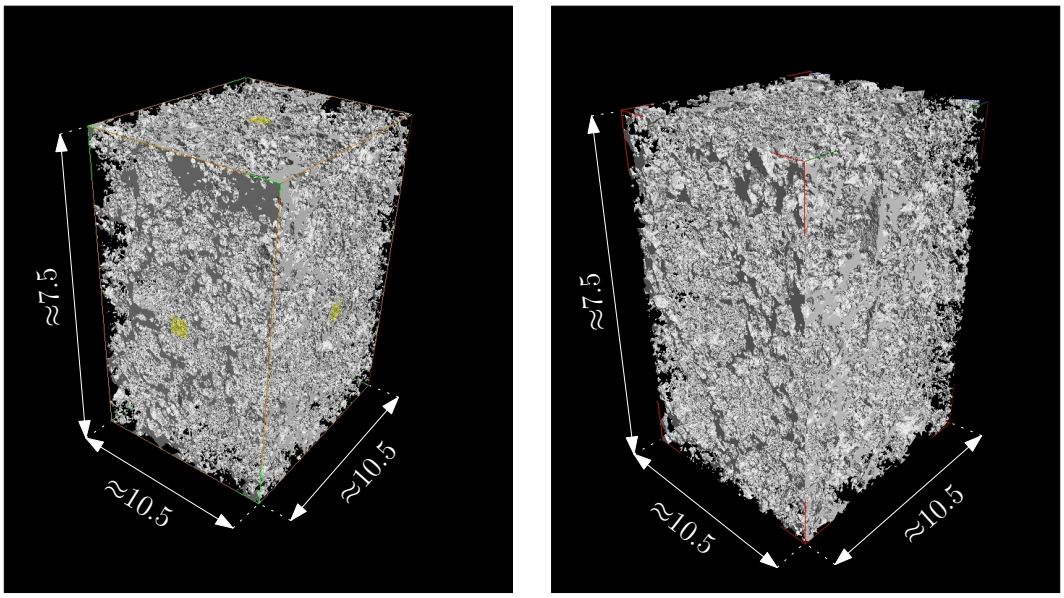

(a) (b)

Figure 4: Reconstructed 3-D pore network for single-layer specimens as detected using XRCT IsoData thresholding: a) top layer of specimen 13d; b) top layer of specimen 15d

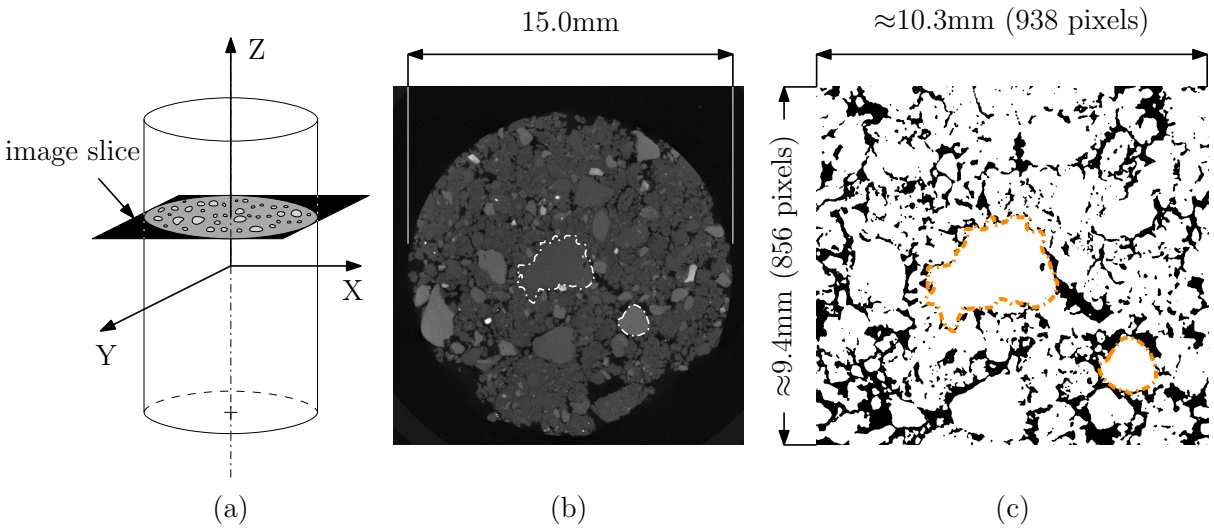

Figure 5: Example of XRCT images: a) specimen axes; b) XY-slice pre-processing; c) XY-slice post-processing. Outlines of particles seen in (b) have been outlined in (c).

thresholding process

1) delete first and last 100 images to prevent shadowing

2) import image sequence

3) analyse → set scale → 1 pixel = 11 microns

4) image → type → 8 bit (needed for thresholding to work)

5) edit → selection → specify (938 x 856 pixels, manually centre, check to see if all images OK)

6) image → crop

7) image → adjust → brightness/contrast (change min/max values to bracket intensity range)

8) process → filters → median (2 pixels)

9) image → adjust → brightness/contrast (change min/max values to bracket intensity range)

10) image → adjust → threshold (isodata, auto)

11) process → noise → remove outliers (2.0, 50, dark)

— *if necessary* —

12) process → binary → fill holes

13) file → save as → image sequence

analysis stages

pore area data

14) analyse → set measurements (choose appropriate parameters)

15) analyse → analyse particles (1089-infinity, 0.00–1.00 circularity, display results, summarise)

fractal data:

16) plugins → fractal analysis → FracLac 2.5 release 1e

- standard box count →
  - grid positions: 5
  - binary or grayscale: use binary
  - background colour: let program decide
  - type of series: use default box sizes
  - sizes per series: 0
  - minimum size: 1
  - maximum box size: 45% ROI
  - find the minimum cover
  - remaining options: ALL deselected
- scan image stack or ROI

Figure 6: Flowchart of image processing algorithm (using ImageJ software)

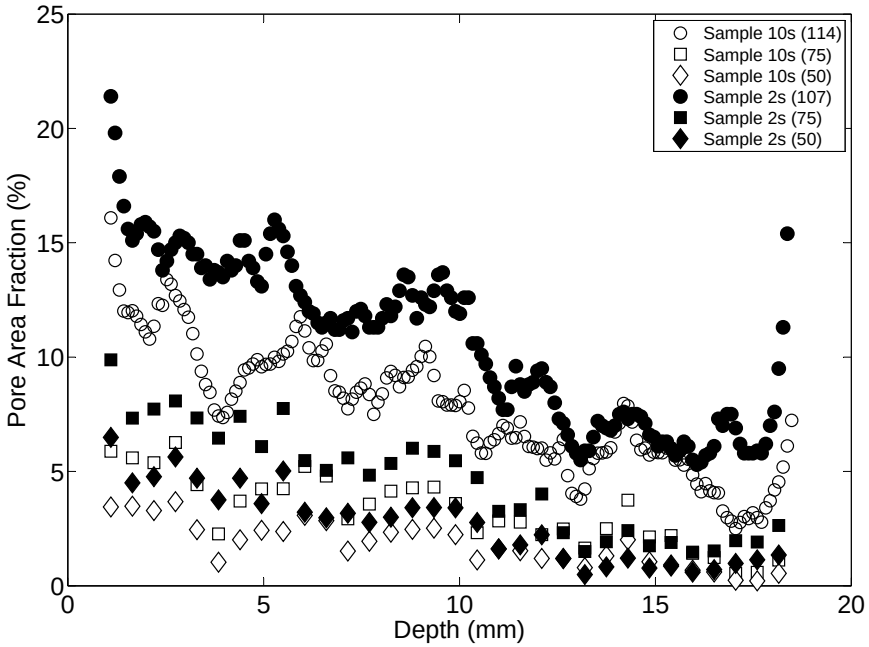

Figure 7: Change in calculated PAF with depth for different threshold intensity values (given in parentheses)

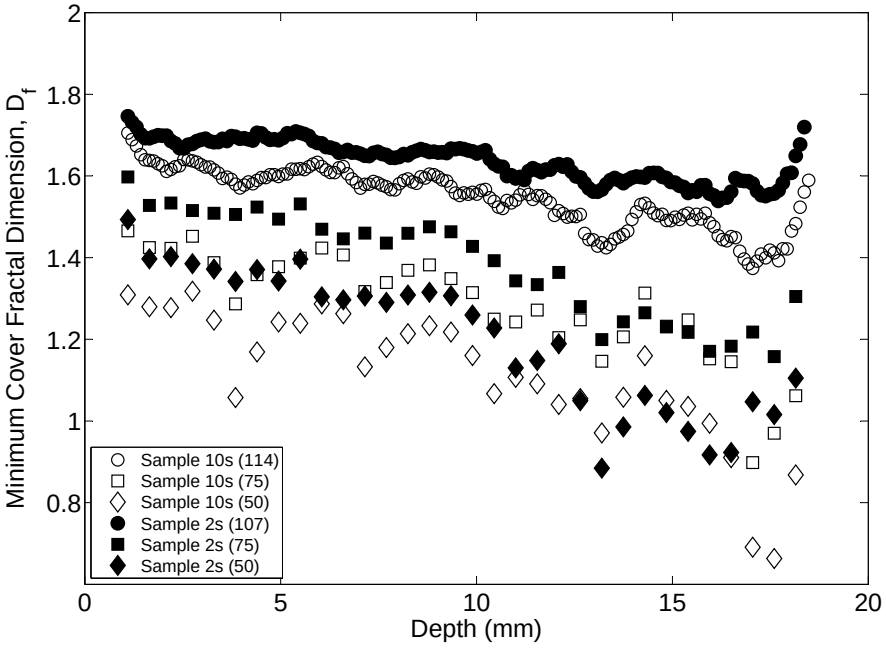

Figure 8: Change in calculated D_f with depth for different threshold intensity values (given in parentheses)

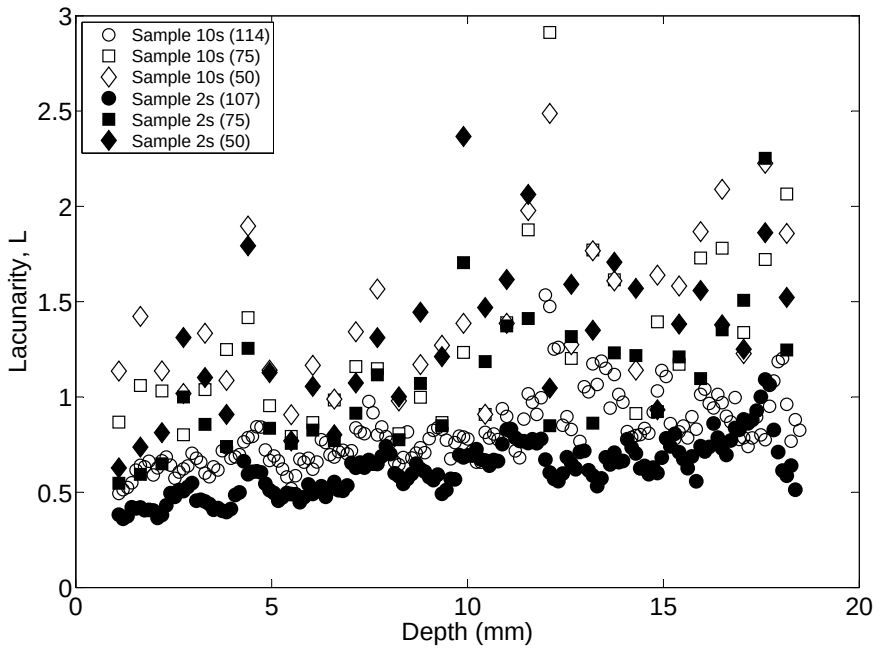

Figure 9: Change in calculated L with depth for different threshold intensity values (given in parentheses)

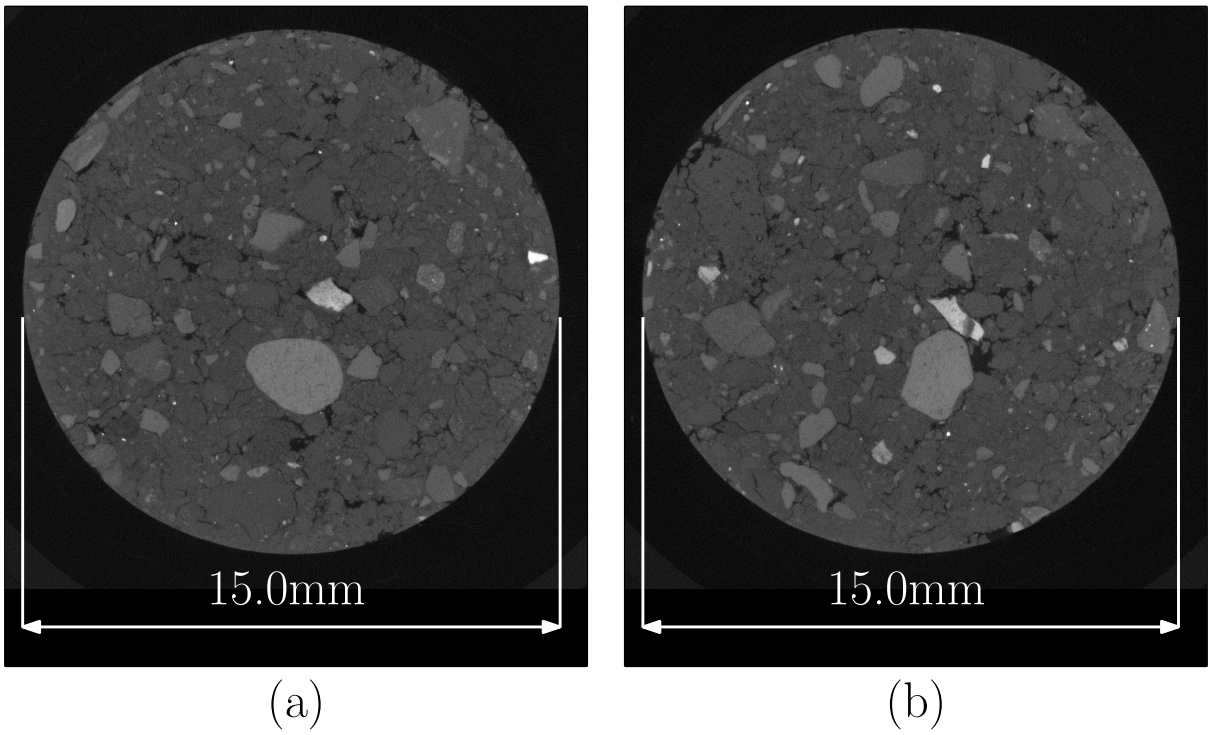

Figure 10: XRCT images taken at: a) 16500 μm; and b) 17379 μm

Figure 11: Large particle present in specimen 10s at 13090 μm: a) XRCT image; b) threshold intensity of 50; c) threshold intensity of 75; d) threshold intensity of 114 (IsoData value).

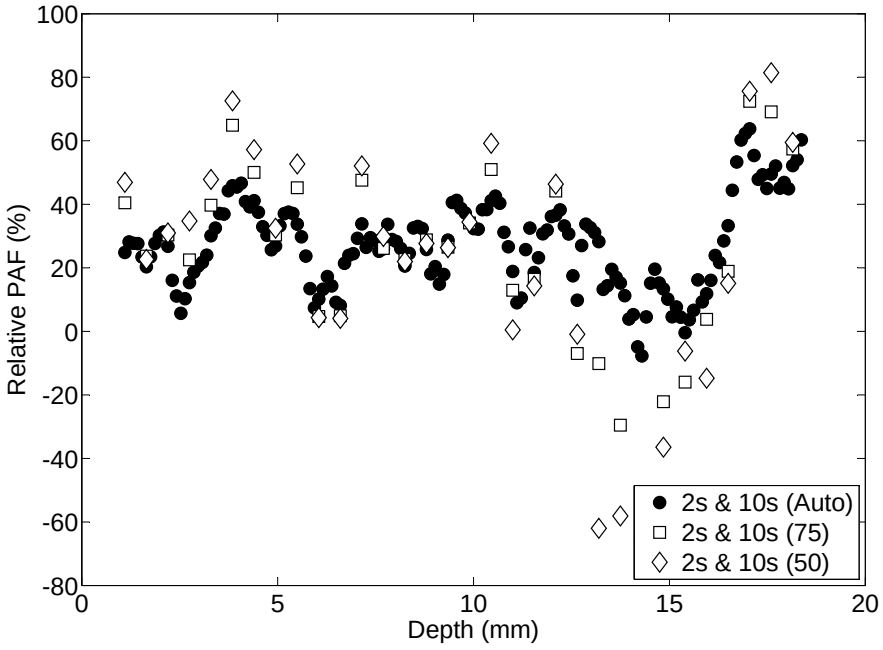

Figure 12: Change in calculated relative PAF with depth for different threshold intensity values

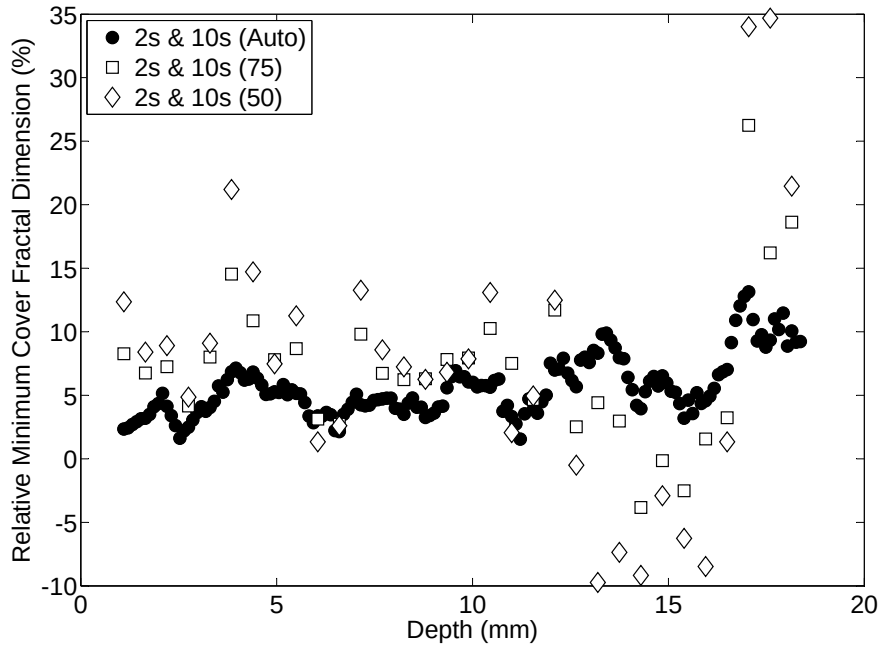

Figure 13: Change in calculated relative D_f with depth for different threshold intensity values

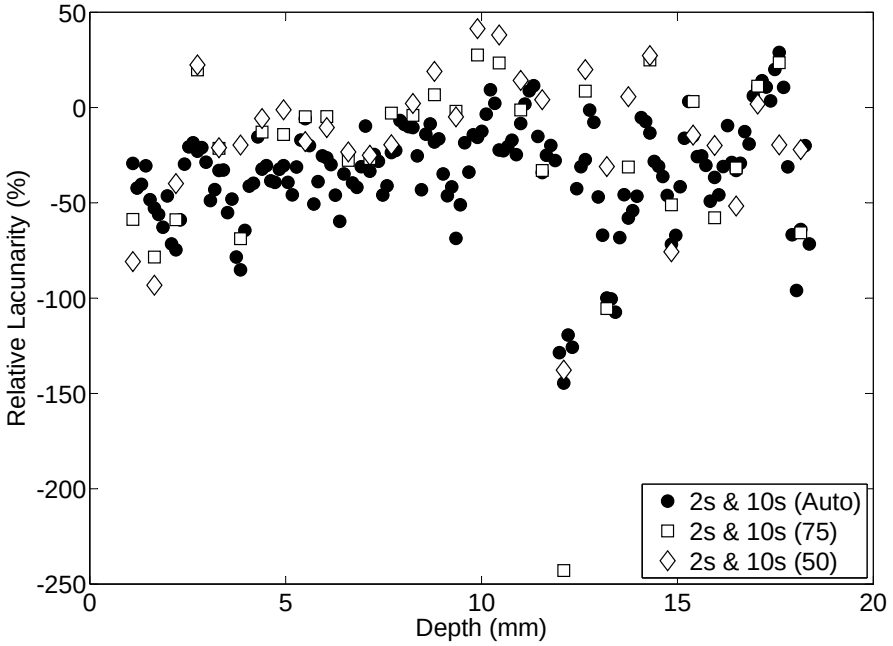

Figure 14: Change in calculated relative L with depth for different threshold intensity values

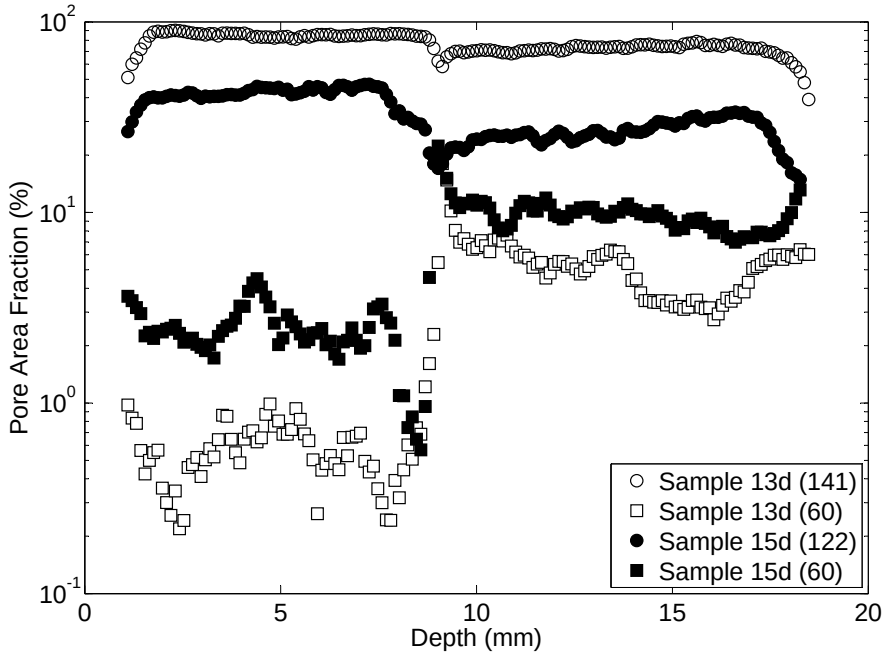

Figure 15: Change in pore area fraction with depth for specimens 13d and 15d for different threshold intensity values

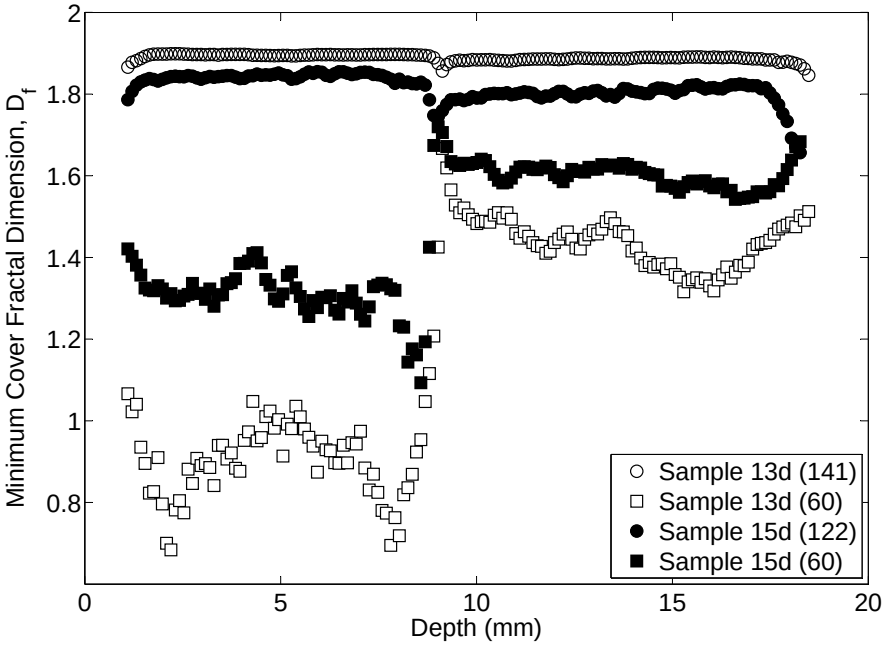

Figure 16: Change in minimum cover fractal dimension with depth for specimens 13d and 15d for different threshold intensity values

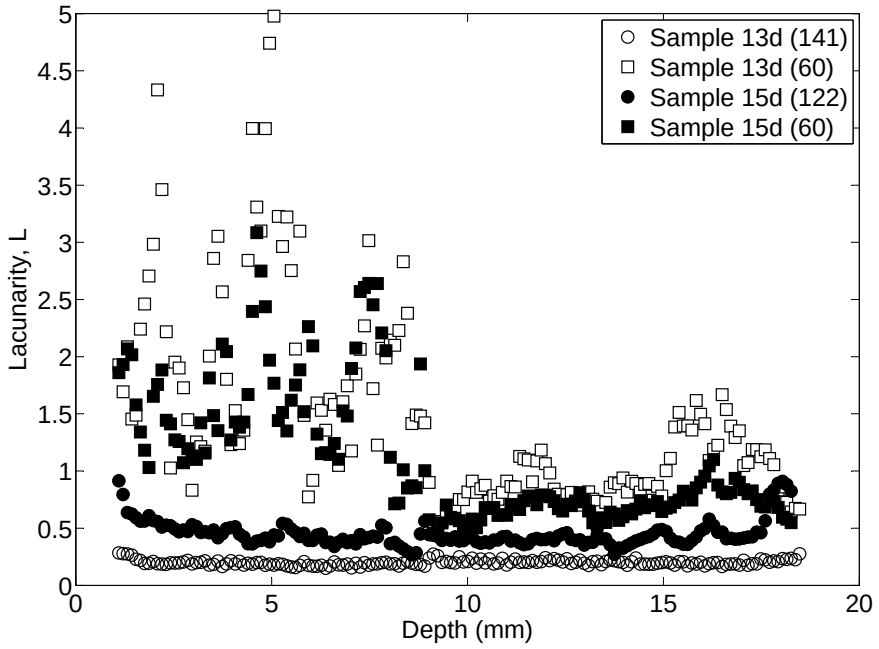

Figure 17: Change in lacunarity with depth for specimens 13d and 15d for different threshold intensity values

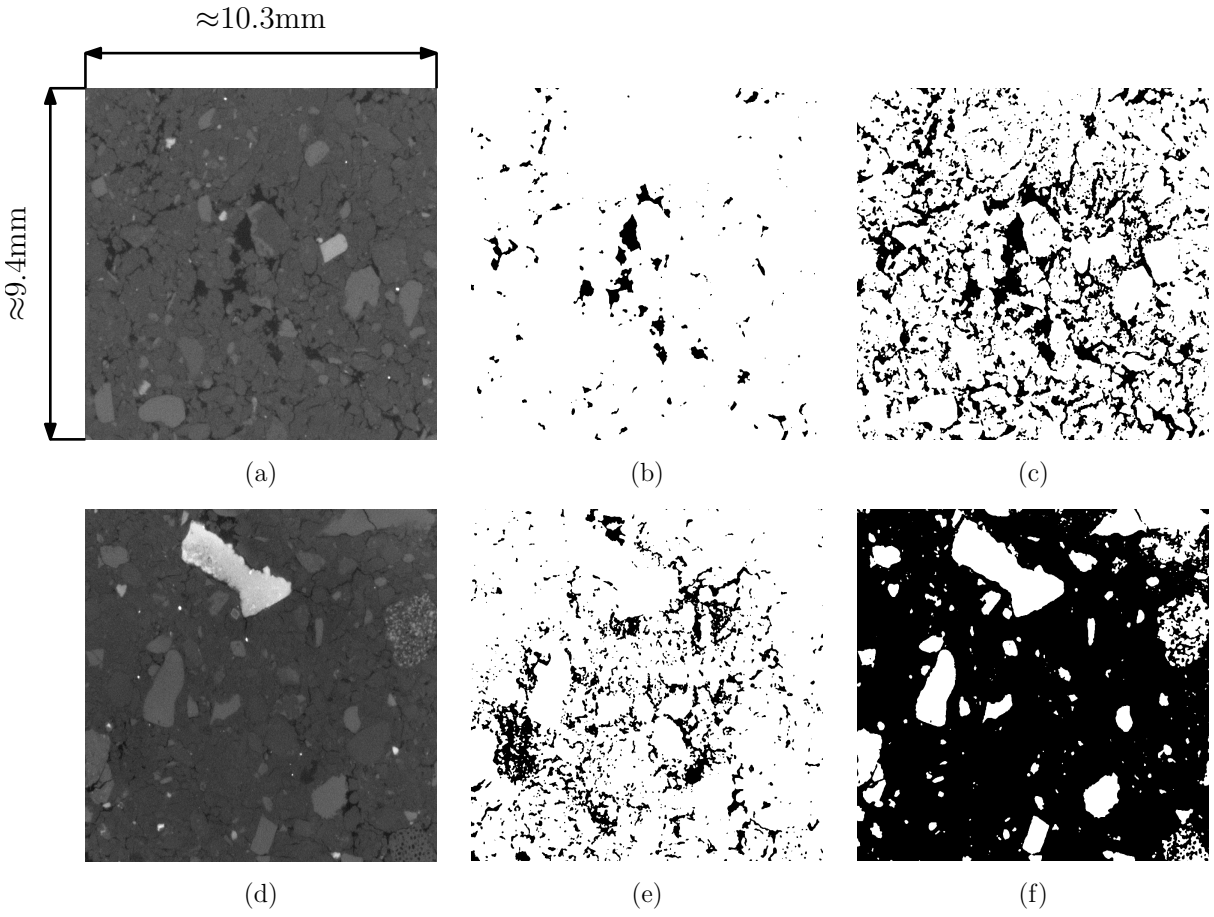

Figure 18: Effect of changing the threshold value on the resulting binary images for specimen 13d: a) original image; b) analysed using threshold value of 60; c) analysed using IsoData threshold value; d) original image; e) analysed using threshold value of 60; f) analysed using IsoData threshold value.

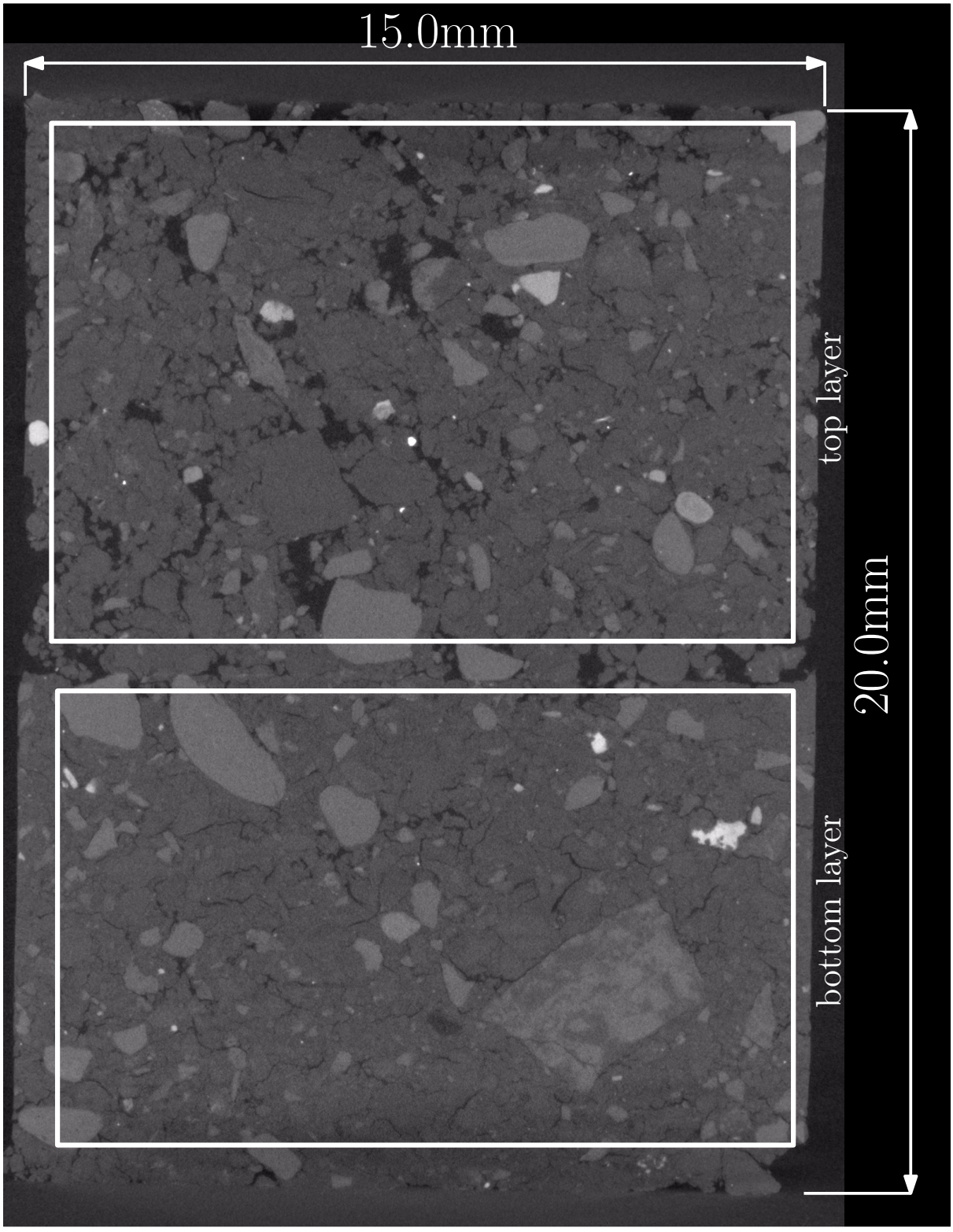

Figure 19: XZ-plane central section of specimen 13d

Table 1: OWC, $\rho_{d_{max}}$ and $\rho_{b_{max}}$ for RE soil mix

OWC (%)	$\rho_{d_{max}}$ (kg/m^3)	$\rho_{b_{max}}$ (kg/m^3)
12.0	1918.1	2147.0

Table 2: Specimen preparation

Specimen	Layers	Applied load (% of UCS)	IsoData Thresholding value (intensity)
2s	1	85	107
10s	1	25	114
13d	2	0	141
15d	2	0	122